PERGAMON

International Journal of Solids and Structures 39 (2002) 1919–1947

INTERNATIONAL JOURNAL OF SOLIDS and STRUCTURES

www.elsevier.com/locate/ijsolstr

Response and failure of a double-shear beam subjected to mass impact

Q.M. Li [a], N. Jones [b,*]

[a] School of Civil and Environmental Engineering, Nanyang Technological University, Nanyang Avenue, Singapore 639798, Singapore
[b] Department of Mechanical Engineering, Impact Research Centre, University of Liverpool, Brownlow Street, Liverpool L69 3GH, UK

Received 15 November 2000; received in revised form 26 November 2001

Abstract

Experimental results are reported for the response and failure of a notched double-shear (DS) beam made from BS970/En24 medium carbon steel alloy when subjected to a mass impact loading. Mechanical properties and constitutive equations were obtained from quasi-static, dynamic and temperature tests on the beam material. Response and failure features were recorded for impact velocities between 30 and 110 m s^{-1}. A failure mode transition was observed between a ductile tensile rupture failure and an adiabatic shear banding failure. This test method could be used for studying shear stress–strain relations over a broad range of strain rates and for investigating different failure modes and their transitions. Finite-element numerical simulations were conducted for the response and failure in the notch section of the DS beam. Calibration factors were obtained, which may be used to calculate the actual stress and strain at the mid-point of a notch section in terms of the nominal values. Isothermal and adiabatic conditions obtained from a dimensional analysis were examined with the aid of FE simulations. An analytical model is used to predict the central block motions of DS beams and gives good agreement with experimental results. Various ductile fracture failure criteria were examined, among which the generalised plastic work density failure criterion leads to successful predictions for the ductile tensile failure within the notch section. © 2002 Elsevier Science Ltd. All rights reserved.

Keywords: Notched beam; Mass impact; Failure mode transition; Finite element simulation

---

1. Introduction

It is well known that pure shear material tests conducted at different strain rates and temperatures can provide fundamental information for developing material constitutive equations, as well as investigating shear fracture and adiabatic shear banding phenomena. Most experimental studies on dynamic material properties and adiabatic shear banding were conducted by using split Hopkinson torsional bar (SHTB) and pressure–shear impact (PSI) techniques. However, the strain rate limitation for SHTB ($\sim 10^3$ s^{-1}) and PSI ($>10^4$ s^{-1}) actually introduce many difficulties for the systematic investigation of material dynamic behaviour in the same experimental configuration over a broad range of strain rates (Klepaczko, 1994a).

---

[*] Corresponding author. Tel.: +44-151-794-4858; fax: +44-151-794-4848.
E-mail address: norman.jones@liv.ac.uk (N. Jones).

PII: S0020-7683(02)00004-5

Nomenclature

b, h	width and thickness of a notch section
d_p	pad thickness defined in Fig. 9 and given in Table 5
e_i, e_a	defined in Eq. (12)
m, m_p, M	masses of the steel pad, central block and projectile, respectively
t	time
t_1	response time for first phase of central block motion determined by Eq. (20)
t_c	characteristic response time
t_{cd}	defined by first term of Eq. (15)
t_T	total loading time in Tables 6 and 7
w^p, w_c^p	generalised plastic work density and its critical value
x_c	characteristic length of a material
A, B_1, B_2	material parameters in Eq. (5)
A_s	transverse cross-sectional area of the notch section in DS beam, i.e., $A_s = bh$
C_v	specific heat
D, q	material parameters in Cowper–Symonds relationship in Eq. (7)
E	Young's modulus
F, F_1, F_2, F_3	functions in constitutive equation (3)
K_v	heat conductivity
L_s, L_{sf}	initial and final specimen lengths in SHPB test
M_1, M_2, M_3, M_4	steel pad mass listed in Table 5
Q	transverse shear force on the cross-section of a notch
T	temperature
T_c	characteristic temperature
T_i, T_a	isothermal temperature in first term of Eq. (12) and adiabatic temperature given by Eq. (13)
T_m, T_r	melting and room temperatures
T_{us}	temperature at the upper-shear notch corner in Table 8
T_{usa}	adiabatic temperature at the upper-shear notch corner in Table 8, calculated by Eq. (13)
T_L	total loading time in SHPB test
V_i	impact velocity of the projectile
V_k	internal variables
V_0	initial velocity of the central block, determined by Eq. (16)
W_b, W_s	defined in Eq. (9) and Fig. 9
α_1,α_2	calibration factors for shear stress and shear strain
β	Taylor–Quinney coefficient
γ, $\dot{\gamma}$	engineering shear strain and its rate
$\dot{\gamma}_c$	characteristic strain rate
$\dot{\gamma}_{c1}$	defined by second term of Eq. (15)
γ_n, $\dot{\gamma}_n$	nominal engineering shear strain and its rate
ε_e, $\dot{\varepsilon}_e$	equivalent strain and strain rate
ε^p, $\dot{\varepsilon}^p$	plastic strain and strain rate in uniaxial tensile test
$\dot{\varepsilon}$	average plastic strain rate in SHPB test
ε_{Ef}	engineering strain at failure

ε_{N0f}	zero gauge length true strain at failure defined in Table 3
ρ	material density
σ	flow stress in uniaxial tension
σ_0	yield stress in uniaxial tension
σ_d	dynamic flow stress
σ_e	von-Mises equivalent stress
σ_H	hydrostatic stress, i.e., $(\sigma_1 + \sigma_2 + \sigma_3)/3$
σ_{Tf}	true stress at failure in uniaxial tension
τ	shear stress
τ_c	characteristic shear stress
τ_n	nominal shear stress
τ_{st}	shear stress in quasi-static loading
$\varDelta$	notch width
$\varDelta_0$, $\varDelta_f$	defined in Eq. (9) and Fig. 9
Δt	incremental time for simulation in Tables 6 and 7

A double-notch shear (DS) specimen can be used at low, medium and high-strain rates in shear. This specimen was first introduced by Ferguson et al. (1967) to study the dynamic plasticity of single crystals. Later the DS specimen was tested using a Hopkinson bar by Campbell and Ferguson (1970), where nominal strain rates in excess of 10^4 s^{-1} were achieved with impact velocities from 1.2 to 11.0 m s^{-1}. However, the determination of the shear strains in the Campbell and Ferguson (1970) tests were prone to large errors when they are higher than a few percent due to the non-uniform shear deformation distributions in the notch section and severe plastic deformations at the specimen supports, as shown by Ruiz et al. (1991) using photoelastic observations and finite element simulations. It was also shown that the distribution of shear stresses in the notch section (or gauge section) does not vary much within the range of small strains, but the stress concentration is quite high at the corners of a 0.84 mm wide square notch.

A modified double-shear (MDS) technique was proposed by Klepaczko (1994b) to overcome these shortcomings. A direct impact of a flat projectile on the MDS specimen allows the shear strain rate in the gauge length to change with the impact velocity. The proposed MDS geometry has a wider gauge length, $l_s = 2.0$ mm (previously 0.84 mm in Ferguson et al. (1967), Campbell and Ferguson (1970), and Ruiz et al. (1991)), and a round corner which reduces substantially the stress concentrations near the notch corners. The specimen ends were designed to be longer than before, and were clamped to the transmitter tube to prevent rotations. A MDS specimen made from a low alloy steel XC18 (French Standard) was analyzed statically at different plastic deformations using a FE method (Klepaczko, 1994b) in order to determine the calibration factor to correct the effects of a non-uniform shear field in the notch section. This experimental technique was also used to investigate the combined strain rate and temperature dependence of the shear flow stress (Rusinek and Klepaczko, 2001).

Although these studies have used a DS specimen as a standard material test technique at various strain rates, it is not a mature technique when compared with the uniaxial tension or split Hopkinson pressure bar (SHPB) techniques. Further studies are necessary to obtain a systematic and complete description of the relationships between the shear stress/strain in the main part of the gauge section and the measurable force/displacement, which are crucial for calculating the shear stress and shear strain. Temperature effects might be important for high-strain rate tests and it is necessary to check its influence on the deformation of a DS specimen.

Another interesting topic for a DS test is the initiation of various failure modes at the notch corners, where a stress concentration is evident (even for a MDS specimen), which include both rupture and adiabatic shearing mechanisms. The impact behaviour of DS specimens made from aluminum alloy and mild steel with sharp triangular notches were studied by Jouri and Jones (1988). Only rupture failure was observed for velocities up to 12 $\mathrm{m\,s^{-1}}$. However, Kalthoff and Winkler (1987) and Kalthoff (1990, 2000) observed a failure transition in a specimen with two parallel edge notches when impact velocities varied from 50 to 100 $\mathrm{m\,s^{-1}}$. This behaviour implies that a transition between rupture and adiabatic shearing failures in a given DS specimen might appear with increasing impact velocities depending on the notch tip radius and material properties. Rupture and adiabatic shearing are controlled by different criteria, so that it is important to determine the associated transition conditions.

In the present study, a DS beam having a similar geometry (except the width of the gauge section) to Klepaczko (1994b) has been subjected to impact velocities within the range of 30–110 $\mathrm{m\,s^{-1}}$. Material properties including strain rate and temperature effects were obtained experimentally and were incorporated into a thermal-visco-plastic constitutive equation. Responses and failure modes have been recorded. These experimental results were analyzed and simulated using numerical and analytical methods. Details of material deformation, temperature changes and failure initiations in a DS beam are discussed, which is of interest for studying the dynamic properties and failure criteria of materials.

2. Material properties

2.1. Physical properties

A BS970/En24 (equivalent to AISI-4340 steel) medium carbon steel alloy was used in the tests, which has the percentage composition of C(0.35–0.45)–Cr(1.4)–Mo(0.3)–Ni(1.4) according to the supplier. Other physical properties (at room temperature) are given in Table 1.

The specific heat of the material is 481.2 $\mathrm{J\,K^{-1}\,kg^{-1}}$ from Woolman and Mottram (1966), which is close to the value, $C_v = 477$ $\mathrm{J\,K^{-1}\,kg^{-1}}$, given by Johnson and Cook (1983). The heat conductivity used here is 38.1 $\mathrm{W\,m^{-1}\,K^{-1}}$ from Woolman and Mottram (1966), which is close to the value $K_v = 37.6$ $\mathrm{W\,m^{-1}\,K^{-1}}$ given by Bai and Dodd (1992, p. 305) for a 4340 steel. Both specific heat and heat conductivity vary with temperature as shown in Table 2. The value of C_v in Table 2 is the mean specific heat from 20 °C to the temperature given.

Table 1
Physical properties

ρ ($\mathrm{kg\,m^{-3}}$)	C_v ($\mathrm{J\,K^{-1}\,kg^{-1}}$)	K_v ($\mathrm{W\,m^{-1}\,K^{-1}}$)	T_m (K)	Hardness (Rockwell)
7830	481.2	38.1	1793	RC-21

ρ, T_m: Johnson and Cook (1983); C_v, K_v: Woolman and Mottram (1966); Hardness: from hardness test.

Table 2
Variations of mean specific heat and heat conductivity with temperature (Woolman and Mottram, 1966)

T (°C)	20	100	200	300	400	500	600	700	800	900
C_v ($\mathrm{J\,K^{-1}\,kg^{-1}}$)	481.2	481.2	502.1	514.6	531.4	556.5	585.8	627.6	707.1	690.4
K_v ($\mathrm{W\,m^{-1}\,K^{-1}}$)	38.1	38.1	38.5	38.1	37.2	34.7	32.2	29.3	26.4	27.2

2.2. Constitutive equation

High-strain rate plastic deformation of a material is often described by a thermo-visco-plastic constitutive equation, which links stress with strain, strain rate and temperature. A general form of the rate and temperature dependent flow stress may be expressed as

$$\sigma_e = F(\varepsilon_e, \dot{\varepsilon}_e, T, V_k) \tag{1}$$

for an isotropic material model, in which σ_e and ε_e are von-Mises equivalent stress and strain, T is temperature and V_k are some internal variables, such as a strain hardening parameter. The function F is often identified by either a uniaxial tensile, a uniaxial compressive or a pure shear test.

The strain hardening, strain rate hardening and thermal softening characteristics are represented by the inequalities

$$\frac{\partial F}{\partial \varepsilon_e} > 0, \quad \frac{\partial F}{\partial \dot{\varepsilon}_e} > 0 \quad \text{and} \quad \frac{\partial F}{\partial T} < 0. \tag{2}$$

Strain softening is also possible when void and texture softening mechanisms are more important, as discussed by Zbib and Jubran (1992).

It is difficult to determine the function F by conducting limited experiments without further simplifications. Most proposed constitutive equations employ the following multiplicative form (Johnson and Cook, 1983; Klepaczko, 1994a)

$$\sigma = F(\varepsilon^p, \dot{\varepsilon}^p, T, V_k) = F_1(\varepsilon^p, V_k)F_2(\dot{\varepsilon}^p)F_3(T), \tag{3}$$

where F_1 is determined from a quasi-static tensile test, F_2 is determined from a SHPB constant strain rate test, and F_3 is obtained by a quasi-static and constant-temperature test. When Eq. (3) is determined from uniaxial material tests it may be converted into the general form of Eq. (1) by using equivalent stress and strain definitions. Thus, the material constitutive equation embodies the two idealizations, i.e., (i) the influences of plastic strain, strain rate and temperature on the constitutive equation can be separated into the multiplicative form in Eq. (3), and (ii) the constitutive equation in the terms of equivalent stresses and strains can be obtained from simple uniaxial tests. The second idealization is based on the assumption that the plastic flow of metals is controlled by the von-Mises equivalent stress and strain. The first idealization will be verified in Section 2.3. Meyers (1994) also discussed the uncoupled characteristics of plastic strain from strain rate and temperature.

2.2.1. Quasi-static tensile test

The mechanical properties from the quasi-static tensile tests are summarized in Table 3. Poisson's ratio is assumed to be 0.29. A relationship between the true stress and natural strain for the material is presented in Fig. 1 when considering the influence of a superimposed hydrostatic tensile stress introduced by necking according to Bridgman's formula. A straight-line interpolation is used between the ultimate tensile stress and the final rupture stress. A modification factor for the influence of hydrostatic stress in a tensile test is given by

Table 3
Tensile test results (INSTRON)

	E (GPa)	σ_0 (MPa)	UTS (MPa)	ε_{Ef} (%)	ε_{N0f}(%)	σ_{Tf} (MPa)
SP2	212.8	391.5	719.5	13.44	66.42	1235
SP3	214.5	383.9	711.3	14.28	63.09	1188

$\varepsilon_{N0f} = \ln(A_o/A_f)$, is the zero gauge length true strain, where A_o and A_f are original and final cross-sectional areas of the tensile specimen. ε_{Ef} is the engineering strain at failure. σ_{Tf} is the true stress at failure.

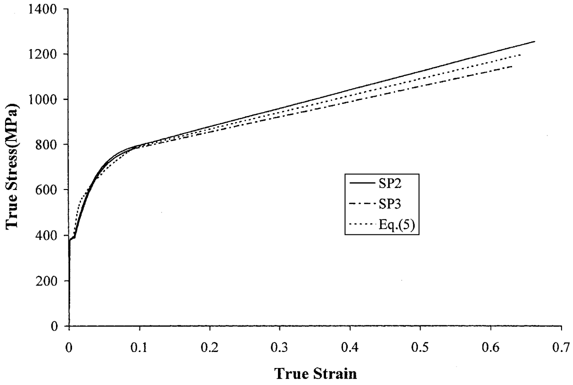

Fig. 1. True stress–strain curves of EN24 steel in uniaxial tension.

$$f_c = 1.0224 - 0.0948\varepsilon_e \tag{4}$$

based on material tests conducted on EN10025 FE430A steel by Alves and Jones (1999a). This modification gives $f_c \approx 0.96$, which is not significant for the present material. However, when the material ductility (ε_{N0f}) is large, the stress value may be reduced more due to the further development of non-uniform stress distributions across the necked cross-section.

The quasi-static true stress–true plastic strain curve in Fig. 1 may be described as

$$\begin{aligned} F_1 &= \sigma_0 \quad \text{for } 0 \leqslant \varepsilon^p < \varepsilon_1^p, \\ F_1 &= \sigma_0 + A(\varepsilon^p - \varepsilon_1^p)^m \quad \text{for } \varepsilon_1^p \leqslant \varepsilon^p < \varepsilon_2^p, \\ F_1 &= B_1 + B_2(\varepsilon^p - \varepsilon_2^p) \quad \text{for } \varepsilon^p \geqslant \varepsilon_2^p, \end{aligned} \tag{5}$$

where $\sigma_0 = 387.7$ MPa, $A = 1182.7$ MPa, $B_1 = 784.1$ MPa, $B_2 = 749.2$ MPa, $m = 0.45$, $\varepsilon_1^p = 0.0065$ and $\varepsilon_2^p = 0.0946$. The plastic strain energy density or the generalised plastic work density, defined by $w^p = \int_0^{\varepsilon_{ij}^p} \sigma_{ij}\,\mathrm{d}\varepsilon_{ij}^p$, up to material failure is 606.64 MJ m^{-3} from Eq. (5) when using the average value of the zero gauge rupture strain, $\varepsilon_{N0f} = 64.76\%$, which is defined in Table 3. Eq. (5) is illustrated in Fig. 1.

2.2.2. Dynamic compressive test

A SHPB was used to obtain the dynamic compressive test results. The average true strain rate is defined by

$$\dot{\varepsilon} = \frac{(L_s - L_{sf})/(\frac{L_s + L_{sf}}{2})}{T_L} \tag{6}$$

in which L_s and L_{sf} are initial and final specimen lengths, $T_L = 155.6$ μs is the total loading time, which depends on the projectile length and elastic wave speed.

The variation of the dynamic yield stress with strain rate is presented in Fig. 2. From these results, the strain rate effect on the yield stress represented by F_2 in Eq. (3) can be described by the Cowper–Symonds relationship, Jones (1997).

$$F_2 = 1 + \left(\frac{\dot{\varepsilon}}{D}\right)^{1/q}, \tag{7}$$

where $q = 4.41$ and $D = 186.7$ s^{-1} fit all tests, as shown in Fig. 2.

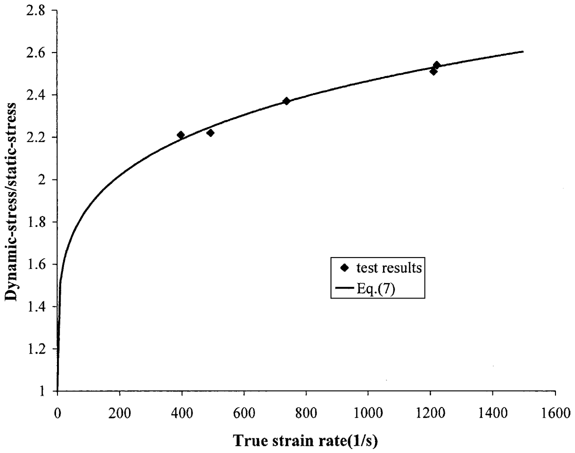

Fig. 2. Variation of dynamic compression yield stress with strain rate.

The parameters D and q in the Cowper–Symonds relationship depend on the magnitude of the plastic strains, as noted by Jones (1989). The strain rate dependence of dynamic flow stress at 12% true plastic strain, which is slightly below the strain at the ultimate tensile stress (13.2%), is obtained using the least square method, i.e., $D = 6948\ \mathrm{s}^{-1}$ and $q = 5.13$, as shown in Table 4. Both sets of parameters obtained above will be verified in Section 2.3 and their influence on DS beam response and failure will be examined in the numerical simulation.

2.2.3. Temperature effects

Quasi-static tensile tests were conducted at various temperatures between room temperature and 500 °C on an INSTRON test machine. The material yield stress decreases with increasing temperature, as shown in Fig. 3. No distinct yielding occurs beyond 320 °C.

The temperature factor in the Johnson–Cook constitutive equation is

$$F_3 = 1 - \left(\frac{T - T_r}{T_m - T_r}\right)^n \tag{8}$$

which is plotted in Fig. 3 against temperature, where a single parameter $n = 0.65$ fits the experimental results.

An increase in temperature also increases material ductility (ε_{N0f}) as shown in Fig. 4. Clearly, the increase of material ductility with temperature is significant, especially when $T > 300$ °C.

Table 4
Dynamic flow stress at 12% plastic strain

No.	ε^p (%)	σ_d (MPa)	σ_d/σ_s[a]	$\dot{\varepsilon}^p$ (s^{-1})
D22	12.02	1342.0	1.721	1216
D13	12.01	1285.0	1.647	741.0
D14	12.02	1350.0	1.731	1226

[a] σ_s is the flow stress at 12% in quasi-static tensile test.

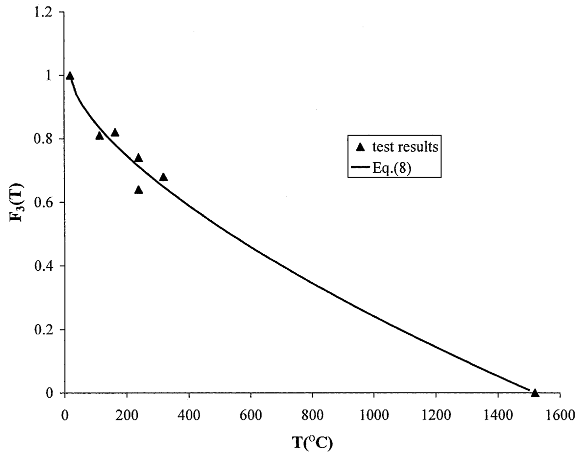

Fig. 3. Variation of yield stress ratio with temperature.

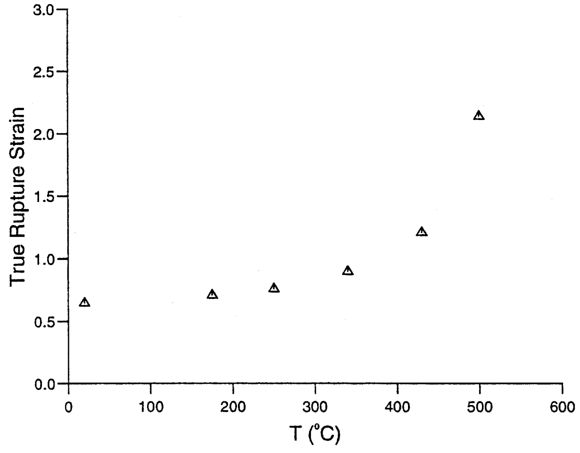

Fig. 4. Variation of zero gauge rupture strain with temperature.

2.3. Verification of the constitutive equation

The function F_2 is the ratio between dynamic and quasi-static yield stresses and is assumed to be independent of the plastic strain. However, it is found that F_2 is plastic strain dependent in Section 2.2.2 where both the flow stresses at 0% and 12% plastic strain are used to obtain two different sets of the parameters, D and q. The two stress–strain predictions can be compared with the stress–strain result from a SHPB test to verify the proposed form of the constitutive equation. Within the current strain rate range, the deformation process in a SHPB test can be idealized as an adiabatic process, which is used to calculate the temperature rise during a test. The actual stress–strain curve in a SHPB test might be influenced by temperature, which, however, is not significant in the present case. Another factor is the variation of strain rate during the loading process. Fig. 5 shows the recorded incident, transmitted and reflected waves in a typical SHPB test at $\dot{\varepsilon} = 1216\ \mathrm{s}^{-1}$. It is evident that the strain rate determined by the reflected wave decreases monotonously from its maximum value to a minimum value that is less than one-half of the

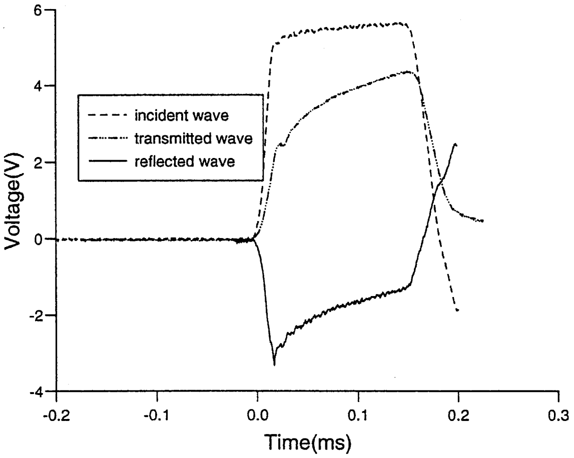

Fig. 5. A typical record of incident, transmitted and reflected waves in a SHPB test.

maximum value. This common feature of non-constant strain rate in a SHPB test has been shown in other publications, for example, Meyers (1994, p. 310). Normally, the variation of strain rate during a test is neglected, and is replaced by an average value. The average strain rate, which is given in Eq. (6) and is used in Eq. (7), is about three-fifths of the maximum value.

When both the temperature rise and the strain rate variation are considered, the predicted results for $D = 186.7\ \mathrm{s}^{-1}$ and $q = 4.41$, and $D = 6948\ \mathrm{s}^{-1}$ and $q = 5.13$ are shown in Fig. 6. Unfortunately, the capability of the SHPB can only produce compressive strains up to 24% in a specimen. The relative differences between the experimental results and the predictions for $D = 186.7\ \mathrm{s}^{-1}$ and $q = 4.41$ at yielding, 10% and 24% plastic strains are 4.3%, 23.9% and 16.3%, respectively. While, the relative differences between the experimental results and the predictions for $D = 6948\ \mathrm{s}^{-1}$ and $q = 5.13$ are 31.4%, 4.4% and 8.2% at yielding, 10% and 24% plastic strains, respectively. In the DS beam test program, most of the material in the notch section of a DS beam has maximum plastic strains between 25% and 50%, as shown later in the numerical simulation. It appears that neither set of parameters D and q offers an accurate description of

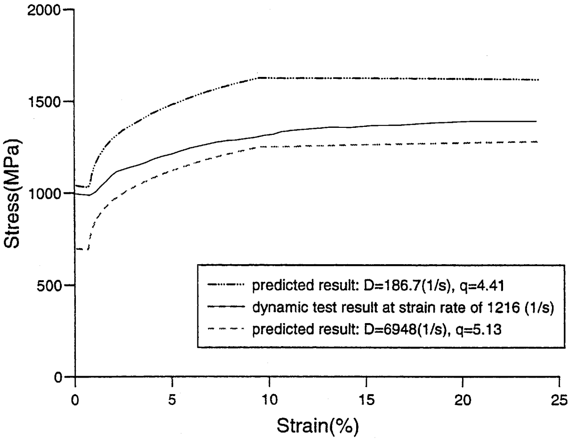

Fig. 6. Comparison between predicted dynamic stress–strain curves and SHPB test result.

the strain rate effect from small to large plastic strains for a particular SHPB test, because the parameters D and q are obtained using the least squares method for a group of varying strain rate tests and a given plastic strain. However, according to a parametric study conducted for the studied problem in Section 4.4, these two sets of parameters lead to a negligible difference for the equivalent strain predictions. Generally speaking, a more accurate and realistic constitutive equation should include the variations of strain rate and temperature effects with plastic strain, i.e. the functions F_2 and F_3 are plastic strain-dependent. However, this would require more material parameters and material tests and introduces considerable complexity for practical applications.

3. Experimental description and results

3.1. Experimental description

A gas gun is used to accelerate the projectile. The actual impact velocities are measured by the photocell system in the experimental arrangement shown in Fig. 7(a). The projectiles are made from an aluminum alloy shell of 20 mm diameter with a hardened steel cap.

A DS beam is clamped by screws on a $255 \times 152 \times 24$ mm^3 steel plate, which itself is clamped firmly on a massive steel block, as shown in Fig. 8. Two hardened beam strips, which are shown in Fig. 8, are used as a stopper, the top surface of which is higher than the top of a DS beam, as shown in Fig. 9. The difference between the stopper level and the top of the DS beam can be calculated using measurements defined in Fig. 9 and given in Table 5. A 10×10 mm^2 steel pad with a given thickness, d_p, is fixed on the top of the central block of the double-shear beam to control the displacement of a projectile, and therefore, the lateral displacement of the central block of a DS beam. The actual thickness of the steel pad and its mass are given in Table 5.

The geometry of the DS beam specimen with a notch width of 2 mm is given in Fig. 7(b).

The specimens were sectioned, ground, polished and etched after a test for microscopic examination.

3.2. General experimental results

The primary experimental results on the DS beams are given in Table 5 for various impact velocities and two different pad thicknesses.

Generally speaking, simple shear dominates the deformations in the notch section. When the impact velocity is low, symmetrical shear deformations are observed in both notch sections. However, with increasing impact velocity, one of the two notches starts to fail. With further increase of the velocity, failures

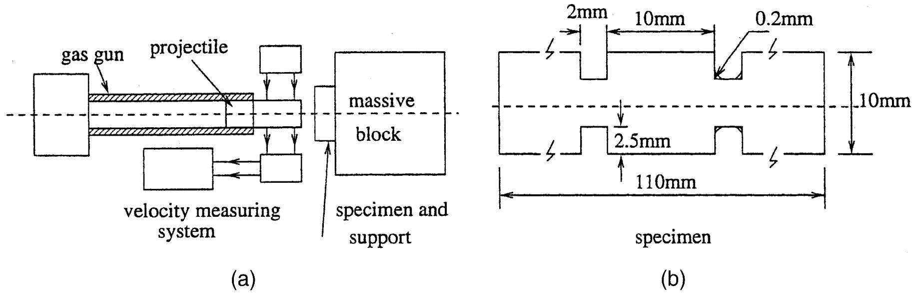

Fig. 7. (a) Experimental arrangement, and (b) test specimen.

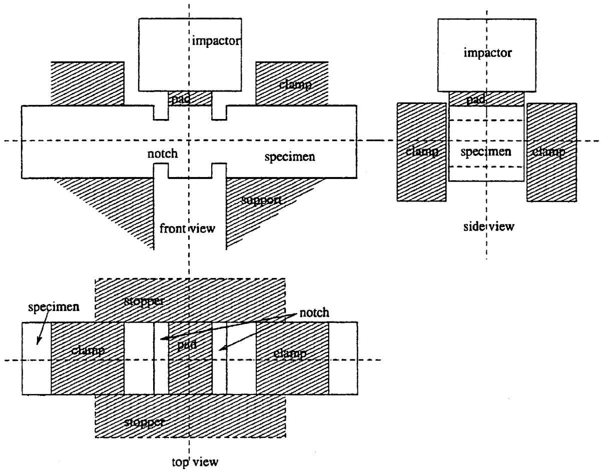

Fig. 8. Clamps and stop plates (note: (1) stoppers are not shown in front view; (2) impactor is not shown in top view, and (3) clamp and support are not shown in side view).

are observed in both notches. Normally, failures are initiated at the corners of a notch. A tensile failure appears at the upper-left (upper right) and lower-right (lower left) corners for the left-hand notch (right-hand notch) of a DS beam (a left-hand notch is referred in the following discussion), which are noted as upper-tensile (UT) and lower-tensile (LT) corners. A shear failure associated normally with adiabatic shear banding is observed at the upper-right and lower-left corners, which are noted as upper-shear (US) and lower-shear (LS) corners in a notch section.

Negligible changes were observed in the pad thickness and the thickness of the central block after impact. However, bending contributions to the displacement of the central block are noticeable. The bending displacements, W_b, defined in Fig. 9, were measured after impact for some specimens, and are given in Table 5 and plotted in Fig. 10 for impact velocities up to 80 m s^{-1}. The bending displacement reaches a maximum value at $V_i \approx 40$–50 m s^{-1}, then decreases due to the failure initiation at the notch corners. An approximate linear relationship between the bending displacement and the impact velocity is given in Fig. 10.

The transverse shear displacement of the central block, W_s, is calculated from

$$W_s = \Delta_f - (d_p - \Delta_0) - W_b \tag{9}$$

in which, Δ_0 is the initial distance from the pad top to the surface of the stop plate measured before impact and Δ_f is the final distance from stop plate surface to the top of central block of DS beam after impact. The measured value of W_b is used when it is available, and the approximate relationship in Fig. 10 is used when it is not. The transverse displacement of the central block according to Eq. (9) is given in Fig. 11 for various impact velocities, and will be compared with the analytical predictions in Section 5.1.

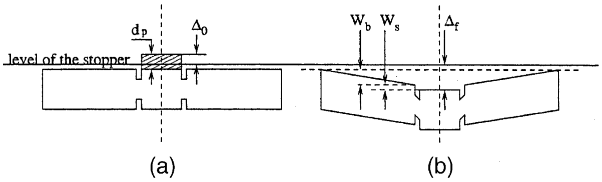

(a) (b)

Fig. 9. Bending and shear displacements in a DS beam. (a) Before impact; (b) after impact.

Table 5
Experimental results of DS beam

No.	V_i (m s^{-1})	d_p (mm)	Δ_0 (mm)	Δ_f (mm)	W_b (mm)	W_s (mm)	Note
NT1	80.5	1.59	1.47	1.44	0.14	1.18	M_1, C, D
NT2	82.8	1.58		1.60	0.06		M_2, C, D
NT3	60.2	1.46	1.35	1.37		1.04	M_2, B, D
NT4	82.8	1.46	1.34	1.64		1.42	M_2, C, D
NT5	47.3	1.46	1.39	1.01	0.29	0.65	M_2, B
NT6	39.2	1.46	1.35	0.81	0.26	0.44	M_2, A
NT7	40.3	1.51	1.40	0.78	0.24	0.43	M_2, A
NT8	52.3	1.49	1.44	1.26		0.96	M_2, B, D
NT9	91.7	1.49	1.46	1.66		1.53	M_2, C, D
NT10	63.38				0.19		M_2, B, D
NT11	70.1	1.58	1.50	1.64		1.38	M_2, C, D
NT12	96.1	1.58	1.45	1.93		1.72	M_2, C, D
NT13	110.3	1.58	1.52	2.00		1.91	M_3, C, D, F
NT21	58.4	1.99	1.87	1.65	0.22	1.31	M_4, C, D
NT22	49.6	1.98	1.88	1.14	0.34	0.70	M_4, B
NT24	78.4	1.98	1.91	2.11	0.01	2.03	M_4, C, D
NT25	41.7	1.98	1.88	0.86	0.32	0.44	M_4, A
NT27	38.7	1.98	1.84	0.76	0.30	0.32	M_4, A
NT28	62.1	1.98	1.84	1.86	0.14	1.58	M_4, C, D
NT29	74.5	1.98	1.91	2.02	0.12	1.83	M_4, C, D
NT30	85.1	1.98	1.86	2.20	0.16	1.92	M_4, C, D
NT31	96.1	1.98	1.87	2.32	0.07	2.14	M_4, C, D
NT32	106.4	1.98	1.91	2.58	0.03	2.48	M_4, C, D, F

$M_1 = 58.3$ g, $M_2 = 62.0$ g, $M_3 = 60.45$ g, $M_4 = 62.38$ g; A—symmetrical shear deformation in notch sections; B—failure in one notch, C—failure in both notches; D—appearance of adiabatic shear band; F—stopper plate (or impact pad or projectile) broken.

3.3. Tensile failure

The two failure mechanisms found within the notches of DS beam specimens are a tensile failure and an adiabatic shear banding failure. Although, there is a small radius of 0.2 mm at each corner of the notch, the stress concentration, and, thus, deformation concentration, is quite severe according to micro-observations

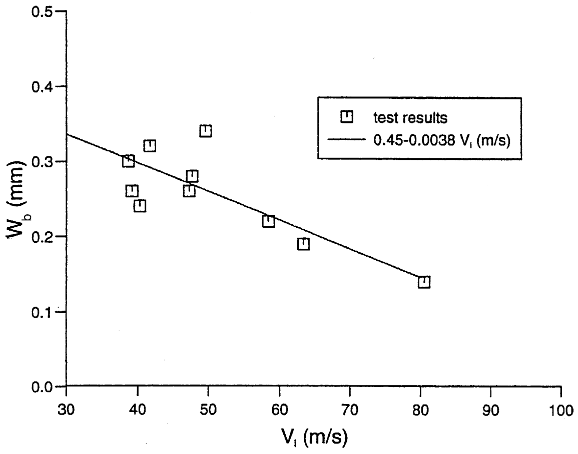

Fig. 10. Variation of bending displacement with impact velocity.

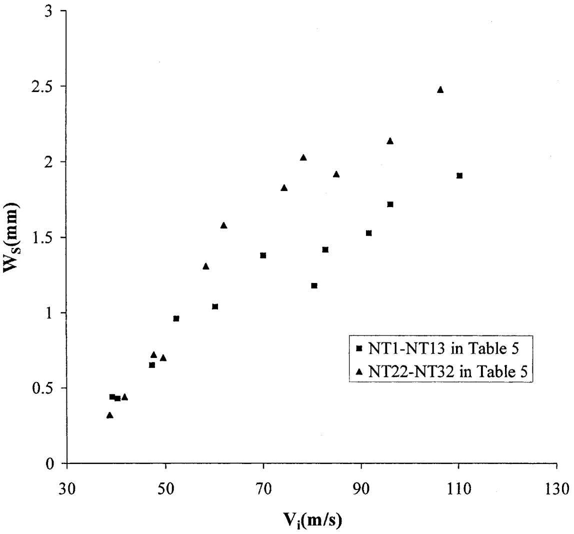

Fig. 11. Variation of transverse displacement of central block with impact velocity.

presented in this section and the FEM simulations in Section 4. Thus, the failure of a DS beam, either a tensile failure or an adiabatic shear banding failure, is initiated from one of its eight corners. This behaviour is different from the behaviour of a thin-walled tube tested in a torsional Hopkinson bar where failure is initiated in the middle of the gauge section, as shown by Marchand and Duffy (1988) for the adiabatic shear band formation process.

Tensile failures are initiated in the tensile domain zones at either the upper-tension (UT) or the lower-tension (LT) corner (or both) when the impact velocity exceeds a critical velocity between 40 and 50 m s^{-1} for both pad thicknesses in the current DS beam tests. Normally, cracks appear in one of the two notches when the impact velocity just exceeds the critical velocity.

Cracks extend at an angle of about 30° to the impact direction. The crack extension length depends mainly on the input kinetic energy, or projectile impact velocity. It appears that the LT corner fails first because many experiments show that cracks at the LT corner extend more than the cracks at the UT corner.

With a further increase of the impact velocity, a third crack is found at the UT corner of the other notch. This occurs because the cracks at the LT corner extend more than the cracks at the UT corner, which decreases the tensile concentration at the LT corner in the other notch. However, with a further increase of impact velocity, tensile failures are found at the UT and LT corners in both notches.

Microscopic examinations were conducted on the crack and its path, as shown in Fig. 12. Crack propagation is irregular on the microscopic scale, which probably could be characterized by fractal patterns with further amplification. Coalesced voids with a characteristic size of order of 100 μm were found at the front of the macroscopic crack. A microscopic tensile stress field over a finite region is consistent with the formation of a macroscopic tensile stress field. The observed macroscopic tensile crack appears to be perpendicular to the principal macroscopic tensile stress. Thus, it is possible that the macroscopic failure pattern can be determined by a macroscopic stress field at the front of a crack during the failure process, although the failure at the microscopic scale is determined by the local microscopic stress field. Thus, any failure phenomena and criteria have their associated spatial scale, which must be specified in a failure analysis.

In addition to the tests in Table 5 on the originally delivered En24 steel, some tests were conducted on a heat treated En24 steel with a hardness HRC 44–46. No tensile failures were found at the UT

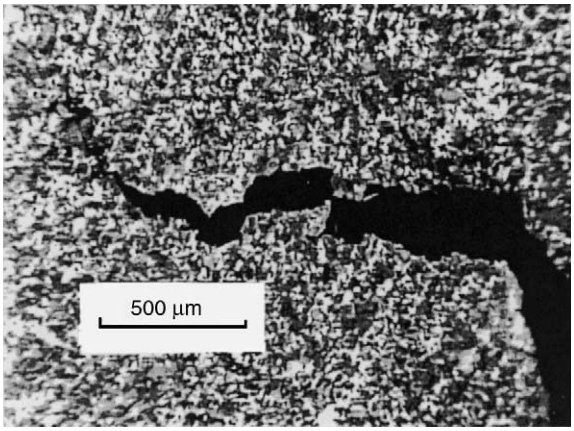

Fig. 12. Microscopic observation of ductile tensile failure for NT21.

and LT corners, but shear failures occurred at the US and LS corners, which will be described in Section 3.5.

3.4. Adiabatic shear bands

Post-test microscopic examinations were conducted on the specimens and adiabatic shear bands were found in front of the cracks at the US and LS corners. An adiabatic shear band at a US corner is shown in Fig. 13(a). It has been claimed in several publications (see Meyers, 1994, p. 448) that shear bands are precursors to fracture, which is true in some situations, as in a SHTB test. However, it is highly possible that a pre-existing crack or an initiated crack may also act as a precursor for the development of an adiabatic shear band, as observed by Kalthoff and Winkler (1987) and Kalthoff (1990, 2000). Shear band initiation in a DS beam is more complicated than in SHTB tube specimen because the local US and LS shear domain zones are not in a state of simple shear. It is also difficult to determine which phenomenon

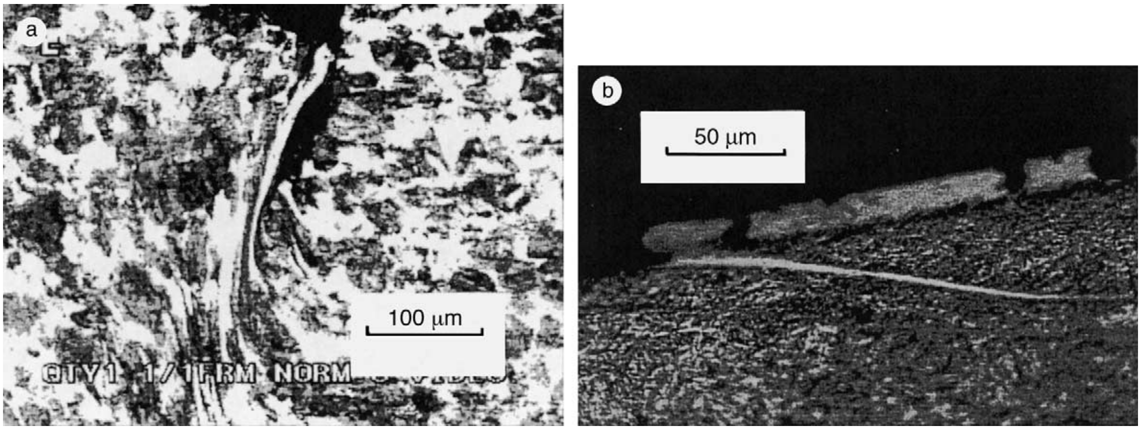

Fig. 13. Microscopic observation of adiabatic shear bands. (a) Shear band in original En24 steel (NT21), (b) shear band in heat treated En24(H) steel with impact velocity $V_i = 52.2\ \mathrm{m\,s^{-1}}$.

(crack or shear band) is initiated first. No matter which phenomenon occurs first, a failure transition between these two failure mechanisms is confirmed in the present test program.

The grains are elongated into narrow strips along the shear band according to the microscopic observations in Fig. 13(a). The elongation of the grains decreases rapidly away from the core of a shear band. The elongation of the grains is much greater than that in a macroscopic tension mode, shown in Fig. 12. It appears that the compressive force created by the macroscopic shear field causes a higher material ductility than for a tensile stress field, which offers the material an opportunity to consume more external energy and increase its temperature. Another reason that a shear stress field can trigger an adiabatic shear band is its simultaneous deformation over a finite material domain, while a tensile failure mode is more likely to be a progressive process which makes it difficult to heat the material up sufficiently to obtain a high ductility before failure occurs. Thus, adiabatic shear banding is more likely to be initiated in a shear stress field. Another factor is the loading rate. It is believed that the reason why grains can experience such high elongation is due to the rapid temperature rise, which triggers a material instability and localizes material deformations in this narrow zone, and, on the other hand, increases the material ductility significantly.

3.5. Discussion

In the current study, both the original delivered En24 and heat treated En24(H) steels were tested. Different features of the shear bands for En24 and En24(H) were observed. The original delivered En24 can be classified as a ductile material, in which severe distortion of the grains was developed in a relatively wide shear band. The En24(H) is more brittle than En24 with a high hardness and strength. The shear band in En24(H) consists of fine grains and has a relatively narrow width compared with En24, as shown in Fig. 13(b) for a typical adiabatic shear band in En24(H). All the EN24(H) test specimens failed completely along a main failure surface, where shear band branches are found. No material data is available for the En24(H) material, so most of the discussion is concentrated on the results obtained using the original delivered En24 material.

A failure transition from a ductile tensile failure to an adiabatic shear banding failure was observed in the present tests. This phenomenon has been studied experimentally by Kalthoff and Winkler (1987) and Kalthoff (1990, 2000) for a sharp notched plate. These two different failures have different mechanisms and failure criteria, which may give different strength predictions for a structure. A similar study on a single notched plate has been presented by Zhou et al. (1996a). They used a high strength C-300 steel and a relatively narrow notch width, and observed that adiabatic shear banding is initiated firstly when the impact velocity is greater than 20 $\mathrm{m\,s^{-1}}$. However, this failure mode is arrested within the specimen and a dynamic crack extends at an angle of about 30° to the impact direction, as observed for the tensile failure mode in the present tests. When the impact velocity is greater than 29 $\mathrm{m\,s^{-1}}$, only an adiabatic shear band propagates throughout the whole ligament of a specimen.

In the present DS beam test, the notch section is relatively larger than those examined in Kalthoff and Winkler (1987), Kalthoff (1990, 2000) and Zhou et al. (1996a). The ductile tensile fracture and adiabatic shear banding occur at different notch corners so that both may occur in a test. It is observed that a low speed impact can generate the conditions for a ductile tensile fracture, while a high-speed impact leads to both ductile tensile fracture and adiabatic shear banding.

A transition from a ductile fracture failure to an adiabatic shear banding failure is also possible in two-dimensional structural elements, such as beams, plates and shells, when subjected to transverse dynamic loading. A theoretical model has been proposed to study the failure mode transition from a ductile shear failure to an adiabatic shear banding failure (Li and Jones, 1999). The response and failure in the notch region of a DS beam presented in this paper are helpful for understanding the transverse shear failures in two-dimensional structural elements.

4. Numerical simulation

4.1. Model description

The physical and mechanical properties of BS970/En24 given in Section 2 are incorporated into the ABAQUS material model. Thermal and mechanical solutions are obtained simultaneously using the coupled temperature–displacement procedure, where temperatures are integrated using a backward difference scheme, and the coupled system is solved using Newton's method. Suitable elements require lower-order (linear) interpolation for temperature than for displacement (linear or parabolic) in order to obtain a compatible variation of thermal and mechanical strains. The element for a four node bi-linear displacement and temperature plane strain element, CPE4T, is used in the present study. More details about the fully coupled temperature–displacement elements in ABAQUS are given in ABAQUS User's Manual (Vol. 1, Section 3.2.3), (ABAQUS, 1996).

Within the option of a coupled-temperature–displacement procedure, the "inelastic heat fraction", "specific heat" and "conductivity" options are needed. The "latent heat" option is unnecessary because there is no phase change in the present problem. Specific heat and thermal conductivity data, which depend on temperature, are given in Section 2, while the Taylor–Quinney coefficient of inelastic heat fraction, β, is taken as 0.9. The parameters in the Cowper–Symonds relationship are $D = 186.7\ \mathrm{s}^{-1}$ and $q = 4.41$. The Johnson and Cook (1983) constitutive equation specified in Section 2 is used as a material model.

An adiabatic analysis is used in cases where rapid mechanical deformation causes heating which has no time to diffuse throughout the material. Generally speaking, the adiabatic assumption can be used for very high-strain rate events, while the isothermal assumption is valid for very low strain rate events. For intermediate strain rate events, heat conduction should be considered. However, the isothermal and adiabatic phenomena are associated with characteristic geometrical scales, for a given problem, in addition to other material parameters. Li and Jones (1999, 2000) have shown that the requirements on the explicit characteristic time and characteristic strain rate for an adiabatic process implies that adiabatic behaviour is a relative concept depending on the geometric scale of the phenomenon. For example, the dynamic deformation process may be considered as an adiabatic phenomenon on the scale of the notch section, but it may be invalid on the scale of the stress concentration zone at the notch corners.

A FE mesh for the DS specimen is shown in Fig. 14. It is not necessary to model the whole specimen shown in Fig. 7(b). In Fig. 14(a), GH is the centre line of the central block. The surface AB is chosen at 2 mm from the notch edge (i.e., DE). The surfaces AB and BC are assumed to be fully clamped, while a normal velocity is imposed on FG and a tangential velocity having the same magnitude is imposed on GH. In order to maintain a constant nominal strain rate, a constant imposed velocity is examined in this section. Each notch has two round corners with radii, 0.2 mm, which are modeled by six elements as shown in Fig. 14(b).

Numerical simulation input data are given in Table 6, where t_T is the total simulation time, Δt is a fixed time increment, W_s is the transverse displacement of the central block corresponding to a maximum nominal shear strain, $\gamma_n = 1.0$, $\dot{\gamma}_n$ is the nominal shear strain rate, V is the imposed velocity at the boundaries FG and GH, and INC is the total number of incremental steps.

4.2. Stress/strain distributions

The nominal shear stress and shear strain can be defined as

$$\tau_n = \frac{Q}{A_s}, \quad \gamma_n = \frac{W_s}{\Delta}, \tag{10}$$

where A_s is the cross-sectional area of the surface DE and Q is the total transverse shear force on a notch cross-section. W_s is the transverse displacement of the central block (the support section has negligible

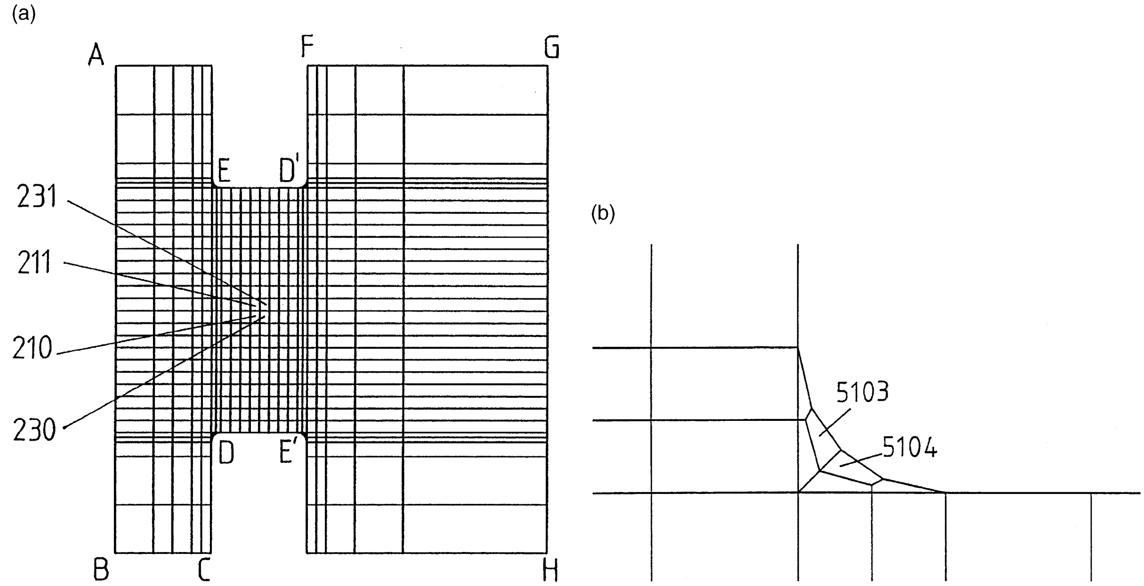

Fig. 14. (a) FE model of a DS notched beam (note: four middle elements in notch are elements 210, 211, 230 and 231); (b) mesh at the notch corner.

Table 6
ABAQUS simulation data-I

No.	$\dot{\gamma}_n$ (s^{-1})	t_T (s)	Δt (s)	INC	W_s (mm)	V (m s^{-1})
DS1	2×10^4	50×10^{-6}	5×10^{-7}	100	2.0	40.0
DS2	5×10^4	20×10^{-6}	2×10^{-7}	100	2.0	100.0
DS4	50	20×10^{-3}	4×10^{-4}	50	2.0	0.1
DS5	5×10^{-2}	20.0	0.1	200	2.0	0.0001

INC is the number of total increments.

permanent displacement), which is the same as the transverse shear displacement of the notch section when the central block is assumed to be rigid, and Δ is the notch width.

It has been shown that there exists a shear zone within the notch section where the shear stress and shear strain distributions do not vary much, although the stress concentration in the corners of a notch are quite high (Klepaczko, 1994b; Rusinek and Klepaczko, 2001). The mid-point of the notch section is always within this uniform shear zone, so that the corresponding shear stress and shear strain could be used to characterize the material response. The actual shear stress (τ)/shear strain (γ) at the mid-point of a notch section is obtained from the nominal stress/strain values, using the expressions

$$\tau = \alpha_1 \tau_n, \quad \text{and} \quad \gamma = \alpha_2 \gamma_n, \tag{11}$$

where α_1 and α_2 are calibration factors which will be determined from the FE simulations.

The test specimens, DS2, DS4 and DS5 in Table 6, have been studied for constant nominal strain rates of 50 000, 50 and 0.05 s^{-1}, respectively. It transpires that the time variations of the transverse shear strain γ at the four elements 210, 211, 230 and 231 in Fig. 14(a) at the mid-point of a notch section are almost identical, which, together with the nominal strains defined by the second term of Eq. (10), can determine the shear strain calibration factor α_2 at various nominal strains, as demonstrated in Fig. 15. This shows that the

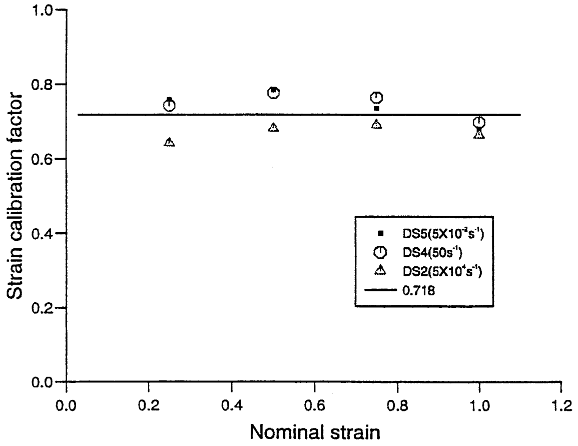

Fig. 15. Variation of shear strain calibration factor with nominal shear strain for different strain rate simulations.

strain calibration factor, α_2, varies only slightly with both plastic strain and strain rate. Thus, a constant value of $\alpha_2 = 0.718$ can be used to obtain the actual shear strain at the mid-point of a notch section from the nominal shear strain.

Stress distributions are also analyzed in these simulations. It is found that the mean shear stress defined by first term of Eq. (10) at the mid-point is almost the same as the mean shear stress at the different locations within a notch section for three different strain rates, despite the fact that the deformations might differ significantly. Therefore, the constant transverse shear force assumption embodied in first term of Eq. (10) is valid within the notch section for these tests.

Klepaczko (1994b) found that the stress calibration factor α_1 has a mean value of 1.2 for $0.05 < \gamma_n < 1.0$ according to a static FEM simulation. Ruiz et al. (1991) also introduced a constant α_1 to calibrate the results, but the actual value of α_1 was not given. Fig. 16 gives the variations of α_1 in first term of Eq. (11) throughout the response period for various strain rate simulations. Generally speaking, α_1 varies within a narrow range from 1.06 to 1.22 for $0 < \gamma_n < 1$ depending on the nominal shear strain and strain rate. It

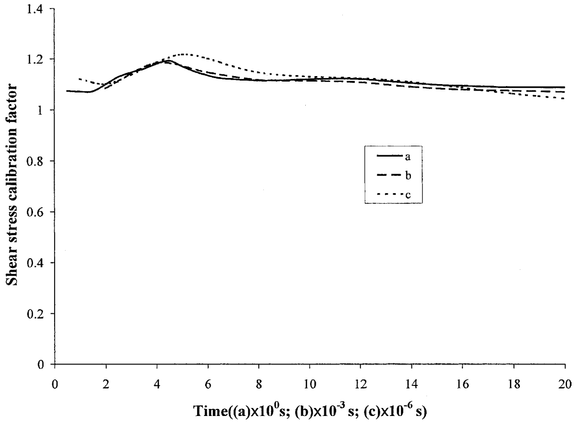

Fig. 16. Variation of shear stress calibration factor with time for different nominal strain rates. (a) DS5 in Table 6 (average value $\alpha_1 = 1.108$); (b) DS4 (average value $\alpha_1 = 1.108$); (c) DS2 (average value $\alpha_1 = 1.118$).

increases from its smallest value at small strains to its maximum at $\gamma_n \approx 0.25$, then decreases for larger strains. This small variation may be neglected from a practical viewpoint by introducing an average value, $\alpha_1 \approx 1.1$, which is independent of both the nominal shear strain and strain rate, and can be used in first term of Eq. (11) to obtain the mid-point shear stress from the nominal shear stress, τ_n, before material failure or thermal instability occurs. It is evident that this value is close to the value ($\alpha_1 = 1.2$) obtained by Klepaczko (1994b) using a static FE simulation.

A more recent publication recommended mean values of 1.142 and 0.65 for α_1 and α_2 due to quasi-static loading (10^{-4} s^{-1}) (Rusinek and Klepaczko, 2001), which is fairly close to the values $\alpha_1 = 1.10$ and $\alpha_2 = 0.718$ obtained in the present paper for strain rates from 5×10^{-2} to 5×10^4 s^{-1}. A DS configuration with these calibration factors could be used for material property tests.

4.3. Temperature effects

The simulations based on the current FE mesh in Fig. 14(a) shows that the isolated boundary AB has no influence on the temperature rise and distribution when $\dot{\gamma}_n \geqslant 10^2$ s^{-1}. When $\dot{\gamma}_n < 10^2$ s^{-1}, the heat conduction across boundaries AB, BC and FG is considered by introducing extra material to approximate the real supports and striker. The temperature rise is significant in most of the present impact tests. Even at a low impact velocity (DS4) with nominal strain rate of 50 s^{-1}, the temperature rise in the shear zone is 139 °C, which has a noticeable influence on the material mechanical properties according to Eq. (8). Thus, it is necessary to consider temperature effects in both the response and failure analyses.

There are three distinct areas within the notch section where the temperature rise is significant, i.e., namely the tensile notch corners (point E and its opposite corner E′ in Fig. 14(a)), shear notch corners (point D and its opposite corner D′) and the main shear zone in the middle of the notch section. Generally speaking, when the strain rate is high (DS1 and DS2), the temperature at a shear notch corner is higher than the temperature at a tensile notch corner. In the low strain rate case (DS4), the main shear zone has the highest temperature up to 139 °C at $\gamma_n = 1.0$, while the temperatures at the shear and tensile notch corners are 106 and 97 °C, respectively, although the generalised plastic work density at both the shear and tensile corners are higher than that in the main shear zone due to the stress and strain concentrations. This occurs because the stress concentration areas at both the shear and tensile notch corners are very small and the heat produced from the dissipative generalised plastic work in these localised areas is soon conducted into the surrounding material when the strain rate is low. The plastic deformation in the main shear zone is almost uniform, and thus, is heated simultaneously from the dissipative generalised plastic work, in which the temperature decrease due to heat conduction is not as significant as at the localised shear and tensile notch corners. It has been shown in Section 2 that the yield stress for this material at 100 °C is 15% lower than the yield stress at room temperature. Therefore, it is recommended that a thermal-coupling analysis with the influence of temperature effects on the material properties is necessary when the characteristic strain rate is over 10^2 s^{-1} in a similar problem.

For the high-strain rate case, the temperature in the main shear zone is lower than the temperatures at both the shear and tensile notch corners. The temperatures at the shear/tensile notch corners for DS1 and DS2 are 859/439 °C and 1050/536 °C, respectively, which are significantly higher than the corresponding temperatures of 246 and 298 °C within their respective main shear zones. This feature indicates that the thermal softening phenomenon is more likely to develop at a shear notch corner, which agrees with the experimental observations.

Isothermal and adiabatic assumptions may simplify calculations when retaining thermal effects in a thermal-coupling dynamic problem. However, it is necessary to obtain the range of validity for strain rates associated with these simplifications. In the present paper, the relative difference of temperatures are defined as follows:

$$e_{\mathrm{i}} = \left\| \frac{T - T_{\mathrm{i}}}{T} \right\| \quad \text{and} \quad e_{\mathrm{a}} = \left\| \frac{T - T_{\mathrm{a}}}{T} \right\| \tag{12}$$

which are used to examine the accuracy of the isothermal and adiabatic simplifications, where T is the temperature at the mid-point of a notch section when mechanical–thermal coupling and heat conduction are considered, $T_{\mathrm{i}} = T_{\mathrm{r}} = 20$ °C is the isothermal temperature at the same location, and T_{a} is the adiabatic temperature calculated from

$$T_{\mathrm{a}} = T_{\mathrm{r}} + \frac{\beta w_{\mathrm{p}}}{\rho C_v}, \tag{13}$$

where, w_{p} is the generalised plastic work density at the mid-point of a notch section calculated using ABAQUS. It should be noted that the "adiabatic analysis procedure" in ABAQUS assumes no heat conduction on any geometrical scale. Under this absolute adiabatic assumption, almost all plastic deformations are concentrated in the shear corners of the notch due to the occurrence of material instability in the notch corner of a DS specimen, which prohibits the propagation of deformations. This does not agree with experimental observations, and thus, the absolute adiabatic assumption is not valid for the present problem. However, adiabatic behaviour is valid within the scale of a whole notch section, i.e., the adiabatic temperature rise can be calculated using Eq. (13), which will be used in the following discussion on the adiabatic behaviour of a DS specimen.

Isothermal and adiabatic conditions have been studied using dimensional analysis in Li and Jones (1999, 2000). The adiabatic assumption could be used if the characteristic response time, t_{c}, and strain rate, $\dot{\gamma}_{\mathrm{c}}$, satisfy

$$t_{\mathrm{c}} \ll t_{\mathrm{cd}}, \quad \text{and} \quad \dot{\gamma}_{\mathrm{c}} \gg \dot{\gamma}_{\mathrm{c1}}, \tag{14}$$

where t_{cd} and $\dot{\gamma}_{\mathrm{c1}}$ are defined in Li and Jones (1999, 2000) as

$$t_{\mathrm{cd}} = \frac{\rho C_v x_{\mathrm{c}}^2}{K_v}, \quad \text{and} \quad \dot{\gamma}_{\mathrm{c1}} = \frac{K_v T_{\mathrm{c}}}{\beta \tau_{\mathrm{L}} x_{\mathrm{c}}^2}, \tag{15}$$

where x_{c} is the characteristic geometrical scale of the studied phenomenon. On the other hand, when $\dot{\gamma}_{\mathrm{c}}$ is much smaller than $\dot{\gamma}_{\mathrm{c1}}$, the isothermal assumption is valid, which means that any temperature rise can be neglected. When $\dot{\gamma}_{\mathrm{c}}$ and $\dot{\gamma}_{\mathrm{c1}}$ are the same order, any heat conduction effects must be considered. These three situations are examined here by using ABAQUS FE simulations. In the present case, $t_{\mathrm{cd}} = 0.4$ s and $\dot{\gamma}_{\mathrm{c1}} = 13.9\ \mathrm{s}^{-1}$ for $x_{\mathrm{c}} = 2$ mm as the notch width, $\beta = 0.9$ as the Taylor–Quinney coefficient, $T_{\mathrm{c}} = 293$ K as the room temperature, $\tau_{\mathrm{c}} = \sigma_0/\sqrt{3} = 223.8$ MPa as the yield shear stress with $\rho = 7830\ \mathrm{kg\,m^{-3}}$, $C_v = 481.2\ \mathrm{J\,K^{-1}\,kg^{-1}}$, $K_v = 38.1\ \mathrm{W\,m^{-1}\,K^{-1}}$ and $\sigma_0 = 387.7$ MPa in Table 1 and Eq. (5). Table 7 gives data on the simulations and Table 8 presents the corresponding results.

Variations of e_{i} and e_{a} with the logarithm of the strain rate are shown in Fig. 17. If the isothermal and adiabatic simplifications are considered acceptable for values of e_{i} and e_{a} which are smaller than 10%, then it is found that isothermal and adiabatic simplifications based on the scale of the notch section can be used for $\dot{\gamma}_{\mathrm{c}} < 10^{-2}\ \mathrm{s}^{-1} \ll \dot{\gamma}_{\mathrm{c1}}$ and $\dot{\gamma}_{\mathrm{c}} > 10\ \mathrm{s}^{-1} \sim \dot{\gamma}_{\mathrm{c1}}$, respectively, and heat conduction should be considered for $\dot{\gamma}_{\mathrm{c}} \sim \dot{\gamma}_{\mathrm{c1}}$. This agrees with the dimensional analysis results in Li and Jones (1999, 2000). It is necessary to recall that the characteristic length, x_{c}, is used as the geometrical scale of a notch section, so that the conclusion is valid on this scale.

The temperature at the US corner of the notch, T_{us}, where a localised stress concentration is severe, is compared in Table 8 with the adiabatic temperature, T_{usa}. Although the relative difference between T_{us} and T_{usa} decreases with increasing strain rate, there is still a large difference at $\dot{\gamma}_{\mathrm{n}} = 10^5\ \mathrm{s}^{-1}$, which means that an adiabatic simplification for the localized stress concentration at the US corner of the notch is not valid for $\dot{\gamma}_{\mathrm{n}} = 10^5\ \mathrm{s}^{-1}$, and for even higher values. A much smaller space scale should be used in the dimensional

Table 7
ABAQUS simulation data-II ($t_{cd} = 0.4$ s, $\dot{\gamma}_{c1} = 13.9$ s^{-1})

No.	$\dot{\gamma}_n$ (s^{-1})	t_T (s)	Δt (s)	INC	W_s (mm)	V (m s^{-1})	Note
TT1	10^{-3}	1000	2	500	2.0	2×10^{-6}	#a
TT2	10^{-2}	100	0.5	200	2.0	2×10^{-5}	#a
TT3	10^{-1}	10	0.1	100	2.0	2×10^{-4}	#a
TT4	1	1	0.01	100	2.0	2×10^{-3}	#a
TT5	10	0.1	0.001	100	2.0	2×10^{-2}	#a
T6	10^{2}	0.01	10^{-4}	100	2.0	0.2	
T7	10^{3}	0.001	10^{-5}	100	2.0	2	
T8	10^{4}	10^{-4}	10^{-6}	100	2.0	20	
T9	10^{5}	10^{-5}	10^{-7}	100	2.0	200	

#a: Extra material is introduced to eliminate boundary effects on heat conduction.

Table 8
Simulation results from Table 7

No.	TT1	TT2	TT3	TT4	TT5	T6	T7	T8	T9
T	20.1	21.4	26.6	46.7	119.6	150	184	230	314
T_a				122	133.9	153	184	230	314
T_{us}				48	76	130	245	437	699
T_{usa}				536	556	610	754	996	1358
e_i (%)	0.5	6.5	24.8	57.2	83.3				
e_a (%)				161.2	12.0	2.0	0.0	0.0	0.0
Note	#b	#b	#b	#b	#b	#b	#c	#c	#c

All temperatures are in °C.
#b: Maximum temperature occurs at the mid-point of notch section when the strain rate is low.
#c: Maximum temperature occurs at the US notch corner for high strain rates.

analysis to find the strain rate range for which the adiabatic simplification is valid in this local area. Further studies on the behaviour of other dynamic problems are necessary in order to verify the validity of the above observations.

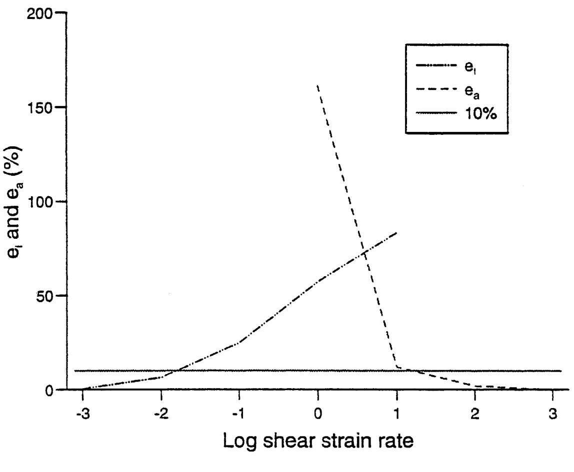

Fig. 17. Variation of e_i and e_a with logarithmic strain rate according to Table 8.

4.4. Verification of plane strain modelling, mesh size and material parameters

The FE model DS1 in Table 6 is simulated by changing the plane strain element type, CPE4T, into a plane stress element type, CPS4T. As expected, the influence is small when employing the plane stress assumption rather than a plane strain one. The maximum relative difference of the von-Mises equivalent stress between using the plane strain and plane stress assumptions is 3.3% after plastic yielding.

Mesh sensitivity was also examined before the final mesh in Fig. 14 was used in the simulations. Based on the mesh configuration in Fig. 14, it was found that further refinement of the mesh in the notch section DED′E′ has a negligible influence on the simulation results. The refinement of the mesh at the notch corners has no influence on the response within notch sections if material failure is not considered. However, the refinement of the mesh at the notch corners may influence the stress and strain predictions at the notch corners.

The six element mesh in the notch corner in Fig. 14(b) is refined first into 14 and, then, 26-element meshes. The predicted generalised plastic work densities at the middle of an UT notch corner using the 14- and 26-element meshes are compared with the same result using the mesh in Fig. 14(b) for DS1 in Table 6. It shows that the final generalised plastic work density based on the average values for the two elements at the middle of a notch corner decreases 7.3% when a 14-element mesh is used. However, further refinement, i.e. 26 elements, leads to an increase of the generalised plastic work density, which reduces the relative difference between the six and 26-element meshes to 5.4%. Thus, the six element mesh in Fig. 14(b) is a reasonable choice. On the other hand, the final selection of the mesh size depends on the characteristic size for the failure criterion. In the present case, the characteristic size of a coalesced void in the front of a macroscopic crack, which is of the order of 100 μm according to the experimental observations, is adopted to determine the mesh size at the notch corner. Thus, the notch corner is modeled finally using the mesh shown in Fig. 14(b) with six elements.

In an actual DS beam test, material failure occurs at a notch corner when the impact velocity is between 40 and 50 m s^{-1}. Thus, DS1 in Table 6 with an imposed boundary velocity of 40 m s^{-1}, is used to verify the influence of parameters D and q in the Cowper–Symonds relation on the response of a DS beam. Two sets of parameters, D and q, which are used in the verification, are based on yielding and 12% strains, as discussed in Section 2.2.2. Their influence on the plastic equivalent strain history is less than 5% in both the notch section and notch corner sections.

5. Discussion

5.1. Analytical model for the central block motion

A DS beam is assumed to be fully supported as indicated in Fig. 8. A projectile travelling with a velocity V_i impacts the impact pad, a square sheet which is made from hardened steel and used to control the displacement of the projectile, as shown in Fig. 8. After impact, the projectile, impact pad and the central block move together with a common velocity when ignoring stress wave propagation effects. The initial velocity of the central block is estimated from linear momentum conservation,

$$V_0 = \frac{M}{M + m + m_p} V_i \tag{16}$$

in which, M is the mass of projectile, m is the mass of central block, and m_p is the mass of impact pad. According to the analysis in Section 4, the transverse shear force is distributed uniformly across the notch section. Thus, the force acting on the boundary of the central block is $\tau_n A_s$, where τ_n is the nominal shear stress defined by first term of Eq. (10), and $A_s = bh$, where b and h are the width and thickness of a notch section. Therefore, force equilibrium requires

$$(M + m + m_p)\frac{dV}{dt} = -2\tau_n A_s, \tag{17}$$

where V is the velocity of the central block of a DS specimen. The initial conditions are

$$V(t = 0) = V_0 \quad \text{and} \quad W_s(t = 0) = 0, \tag{18}$$

where, V_0 is given by Eq. (16) and W_s is the transverse displacement of the central block. After travelling a fixed distance determined by the difference between the level of stopper, and the top of the impact pad, Δ_0, defined in Fig. 9, the projectile is stopped by the surrounding stoppers, and the impact pad, which was glued to the specimen, is separated from the central block. Thus, for later times after $t = t_1$, the equation of motion is

$$m\frac{dV}{dt} = -2\tau_n A_s, \tag{19}$$

where

$$W_s(t = t_1) = \Delta_0 \tag{20}$$

from Eqs. (17) and (18).

Any deformations of the impact pad and projectile are neglected in the above formulation because their stiffness is much larger than the stiffness of a DS specimen. Wave propagation effects in the central block are not considered because the characteristic time of wave propagation in the central block is only about 4 μs that is much shorter than the response time.

The nominal shear strain and shear strain rate at the mid-point of a notch section are

$$\gamma_n = \frac{W_s}{\Delta}, \quad \text{and} \quad \dot{\gamma}_n = \frac{V}{\Delta}, \tag{21}$$

in which, Δ is the width of a notch section.

The shear stress–strain relationship from Eq. (3) can be expressed in the form

$$\tau = \tau_{st}\left(1 + \left(\frac{\dot{\gamma}(s^{-1})}{323.4}\right)^{\frac{1}{4.41}}\right)\left(1 - \frac{(T(^\circ C) - 20)^{0.65}}{116}\right), \tag{22}$$

according to the von-Mises yield condition, i.e. $\tau = \sigma/\sqrt{3}$ and $\gamma = \sqrt{3}\varepsilon$, and where the temperature is obtained from Eq. (13) by using the adiabatic simplification which has been shown to be valid in Section 4 for the present impact velocity range, and τ_{st} is given by

$$\begin{aligned} &\tau_{st} = 223.84 \text{ (MPa)} \quad \text{for } 0 \leqslant \gamma \leqslant 0.01126, \\ &\tau_{st} = 223.84 + 533.29(\gamma - 0.01126)^{0.45} \text{ (MPa)} \quad \text{for } 0.01126 < \gamma \leqslant 0.16, \\ &\tau_{st} = 411.8 + 249.7\gamma \text{ (MPa)} \quad \text{for } \gamma > 0.16. \end{aligned} \tag{23}$$

according to Eq. (5).

The final displacements of a DS beam in Table 5 are compared with the current theoretical predictions in Fig. 18. Generally speaking, the theoretical predictions for both the 1.5 and 2.0 mm pad thickness tests are smaller than the experimental results. One important factor responsible for this phenomenon is the local shear and tensile failures at the notch corners that reduce the transverse strength of the notch section in the test specimens, but which is not considered in the analytical model. However, in general, the agreement between the experimental results and theoretical predictions for the final displacements is fairly reasonable.

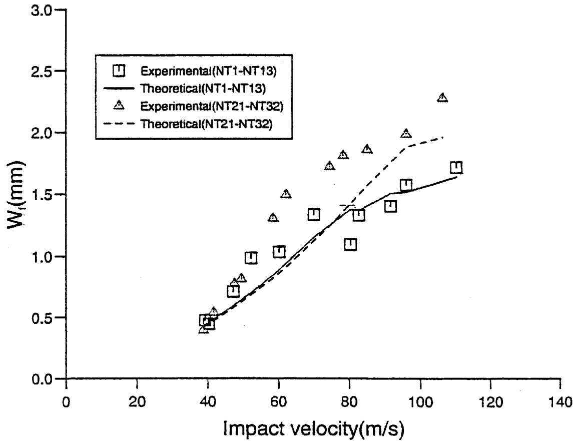

Fig. 18. Comparison between experimental and analytical results for the final transverse displacements of DS beams.

The method proposed in this section will be used to predict the velocity–time history that can be used in the next section to simulate the failure initiation of the DS beam tests.

5.2. Failure initiation criteria

There are various failure criteria that may be used to predict a material ductile failure. Several ductile failure criteria, including both global and local failure criteria, have been examined by Yu and Jones (1997) for the failure of beams subjected to a mass impact loading. An approach combining material and structural experimental results and FE numerical simulations was employed to evaluate the reliability and generality of a failure criterion. It was found that the maximum membrane force in a beam cross-section, as a global failure criterion, is the most promising one for a beam tensile failure. The local failure criteria, i.e., maximum Tresca or von-Mises stress and the maximum generalised plastic work density failure criteria, are worthy of further study for a shear failure. It was suggested by Cockcroft and Latham (1968) that the critical value of the generalised plastic work density failure criterion is practically constant at moderate strain rates, which was used to study the fracture of solid polymers by Vinh and Khalil (1984). Gillemot (1976) and Clift et al. (1987, 1990) used it as failure criterion in various quasi-static situations. Shen and Jones (1992) and Jones and Shen (1993) combined it with the rigid-plastic method to study the impact failure of structural elements. The theoretical foundation of the generalised plastic work density failure criterion and its application is discussed in Li (2001).

In the present paper, seven different local failure criteria are examined, i.e., maximum normal stress failure criterion, maximum shear stress (or Tresca) failure criterion, von-Mises equivalent stress failure criterion, maximum plastic tensile strain failure criterion, equivalent plastic strain failure criterion, maximum plastic shear strain failure criterion and generalised plastic work density failure criterion.

According to the experimental observations in Section 3 on material tensile failure in a DS beam, all tensile failures initiate from the UT and LT notch corners. The critical impact velocity is between 40.3 m s^{-1} (specimen NT7 without failure) and 47.3 m s^{-1} (specimen NT5 with failure), as shown in Table 5. Seven failure criteria will be used to examine the accuracy of the available failure criteria. The maximum values of these failure indices around the critical impact velocity occur at the middle elements in the corner of a notch described in Fig. 14(b). Values associated with the two middle elements (5103 and 5104) are almost the same, and thus, their average value is used. Table 9 gives the predicted values for tests NT5 and NT7 from the ABAQUS FE simulations, which are compared with the measured values reported in Section 2.

Table 9
Critical values of the failure indices ($\beta = 0.9$, $D = 186.7\ \mathrm{s}^{-1}$, $q = 4.41$)

Failure criterion	Material test value	Predicted value (NT7)	Predicted value (NT5)
$\sigma_{\max}$ (MPa)	1211.8	3230.0	3410.0
σ_{Tresca} (MPa)	605.9	1512.0	1595.5
σ_{Mises} (MPa)	1211.8	2619.0	2763.0
$\varepsilon^{\mathrm{p}}_{\max}$	0.648	0.264	0.294
$\varepsilon^{\mathrm{p}}_{\mathrm{eq}}$	0.648[a]	0.231	0.337
$\varepsilon^{\mathrm{p}}_{\max} - \varepsilon^{\mathrm{p}}_{\min}$	0.972[a]	0.461	0.587
W^{p} (MJ m^{-3})	606.64	599.0	816.0

[a] For a plastic incompressible material.

It is observed that the generalised plastic work density failure criterion obtained from a static tensile test provides a reasonable prediction for the initiation of failure. Stress failure values from material tests are smaller than the values at failure in the tensile notch corner, but the actual strain values at failure are higher than the corresponding predicted values. The variations of the maximum values of $\varepsilon^{\mathrm{p}}_{\mathrm{eq}}$ and w^{p} with the impact velocities are calculated using ABAQUS, and compared with the critical values of $\varepsilon^{\mathrm{p}}_{\mathrm{eq}}$ and w^{p}, as shown in Fig. 19. The FE simulation results show that the maximum values of $\varepsilon^{\mathrm{p}}_{\mathrm{eq}}$ and w^{p} occur at the upper tensile corner, which is in contrast with the experimental observations that tensile failures are more likely to be initiated from the LT corner. However, bending effects are not considered in modeling the central block motion in Section 5.1, but would cause the LT corner to fail more easily than the UT corner. The differences in the maximum values for $\varepsilon^{\mathrm{p}}_{\mathrm{eq}}$ and w^{p} are not significant between the UT and LT corners according to the ABAQUS simulations. For example, the maximum values of w^{p} are 652.4 and 576.5 MJ m^{-3} at the UT and LT corners, respectively, when the impact velocity is 40 m s^{-1}. Thus, it is reasonable to use an average value to give the maximum value for the prediction of failure. The critical value of $\varepsilon^{\mathrm{p}}_{\mathrm{eq}}$, $\varepsilon^{\mathrm{p}}_{\mathrm{eqc}}$, is the static natural strain based on the zero gauge length defined in Section 2, which has an average value of 0.648 for EN24 steel. This value increases with temperature, as shown in Fig. 4. The critical value of w^{p}, $w^{\mathrm{p}}_{\mathrm{c}}$, is calculated from the uniaxial true stress–true strain relationship at room temperature given by Eq. (5), while the calculated w^{p} in a numerical simulation is based on a characteristic element length of 100 μm which is the characteristic length of a coalesced void in the front of macroscopic crack, as discussed in Section 3.3.

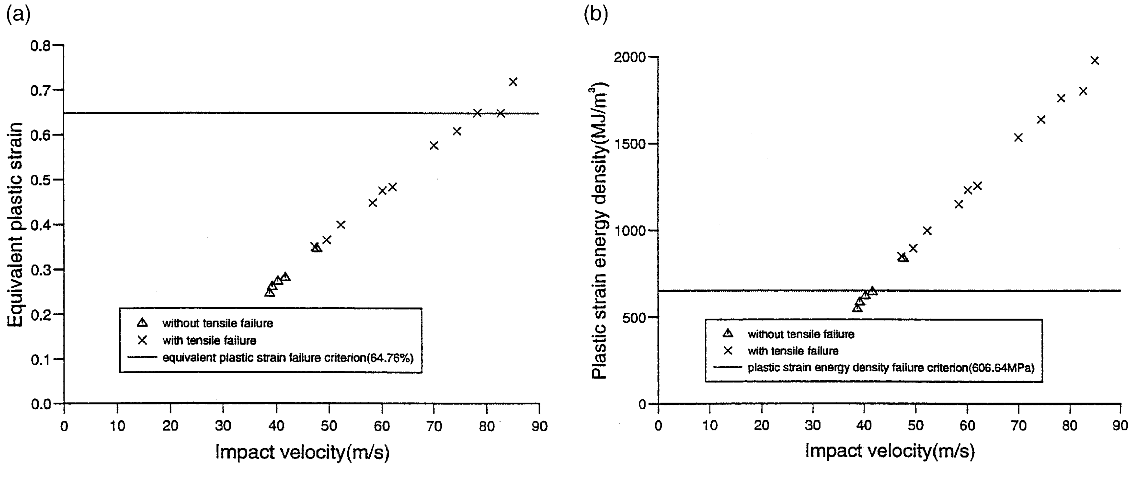

Fig. 19. Predictions of tensile failure initiation in notch section of a DS beam. (a) Equivalent plastic strain; (b) generalised plastic work density.

According to the results from Table 9 and Fig. 19(a), the equivalent strain failure criterion does not agree with the experimental results. The ABAQUS FE analysis predicts that the actual value of ε^{p}_{eqc} at the failure site is between 0.3 and 0.35 corresponding to an average strain rate of $\sim 10^4$ s^{-1}, which is much lower than its quasi-static measurement value. The local temperature at the failure site is about 150 °C when the impact velocity is 45 m s^{-1}, which leads to an increase of ε^{p}_{eqc} of less than 10%. There are two other factors that may contribute to this result, in addition to temperature effect. One is the influence of the strain rate effect on the failure strain, which, although, has not been studied thoroughly, can cause a significant reduction in the rupture strain for some materials, e.g., mild steel (Jones, 1989). Another factor is the stress triaxiality, which may also reduce the failure strain. In a uniaxial tensile test, the value of stress triaxiality, σ_H/σ_e, is 0.33. The time history of the average stress triaxiality at the UT corner is calculated by using ABAQUS, and is shown in Fig. 20 for specimen NT7. The value of σ_H/σ_e is 0.655 at the end of the response, which is almost double the value in a uniaxial tensile test. It has been shown by Alves and Jones (1999b) that the equivalent fracture plastic strain reduces from about 1.0 at $\sigma_H/\sigma_e = 0.4$ to about 0.5 at $\sigma_H/\sigma_e = 0.8$ (see Fig. 9 in Alves and Jones (1999b)). A similar observation is reported by Holmes et al. (1993). Thus, this phenomenon appears to make a potentially important contribution to the reduction of the equivalent plastic strain at failure and the consideration of this phenomenon could provide much better agreement with the experimental results in Fig. 19(a).

w^{p}_{c} from a quasi-static tensile test gives a good estimate for the initiation of tensile failure. The actual failure occurs for w^{p}_{c} between 599 and 816 MJ m^{-3} compared with $w^{p}_{c} = 606.6$ MJ m^{-3} obtained from a static tensile test. Thus, the static critical value of the generalised plastic work density is bounded by the predicted values in an actual failure. This result implies that both the temperature, the strain rate and the triaxiality effects on w^{p}_{c} are small, or mutually cancelling. Thus, the present work shows that the generalised plastic work density failure criterion is a more promising procedure for predicting failure than the other stress and strain type failure criteria examined. It is possible that other failure criteria are applicable when other influencing factors, such as strain rate, temperature and hydrostatic effects, are identified in material failure tests. However, this requires more advanced measuring techniques and additional test work.

5.3. Remarks

It has been shown that adiabatic shear banding appears when the impact velocity approaches 52 m s^{-1}. The location of an adiabatic shear band is either at the US corner or at the LS corner (or both) within the

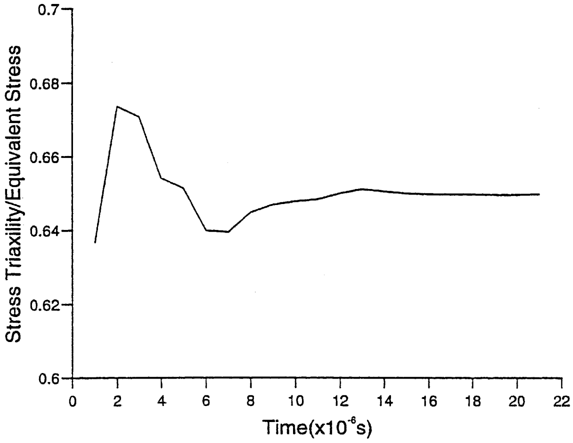

Fig. 20. Variation of stress triaxiality, σ_H/σ_e at the UT corner of specimen NT7 in Table 5.

notch section, where the stress concentration is severe. A shear band normally originates from a non-homogeneous deformation phase followed by a localization phase, which was observed by Marchand and Duffy (1988) who studied the formation of shear bands in a thin-walled steel tube. It has been accepted generally that the maximum shear stress criterion can be used to predict the initiation of the non-homogeneous shear deformation phase (Bai and Dodd, 1992), and thus, has been used as a critical condition for the catastrophic development of an adiabatic shear band. This maximum shear stress criterion was developed originally for a one-dimensional stress problem and it is normally applied for constant strain rate. Batra and Nechitailo (1997) used it for a two-dimensional stress problem. But, in the most general situation, it appears that the critical condition for the initiation of a thermal instability requires

$$d\tau = 0, \quad \text{and} \quad d\dot{\varepsilon}^{p}_{eq} \geqslant 0, \tag{24}$$

where τ is the maximum shear stress component. Further theoretical, experimental and numerical studies are necessary to verify these conditions. The initiation and propagation of an adiabatic shear band in the notch section of a DS beam are not simulated in the present paper. However, interested readers may refer to Zhou et al. (1996a,b), Batra and Nechitailo (1997) and Batra and Gummalla (2000).

6. Conclusions

The response and failure of a DS beam when subjected to a projectile impact are studied in the present paper.

The material constitutive equation, which includes strain hardening, strain rate and temperature effects, was obtained through a series of tests on the DS beam material. Failure modes within the notch section include tensile ductile fracture in the tensile domain region and adiabatic shear banding in the shear domain region. The initiation of these failure modes depends on the impact velocity for a given DS beam, and critical impact velocities were observed for the initiation of ductile tensile fracture and adiabatic shear banding.

With the aid of a FE simulation, the details of the stress and strain distributions in the notch section are obtained, and are used to obtain relationships between the nominal stress/strain values and their actual values in the major shear zone within the notch section. This information is particularly useful when using a DS beam for a dynamic shear test. Temperature effects are discussed in the present analysis by using a coupled-temperature-displacement procedure in ABAQUS.

Due to the high stress intensity at the notch corners in a DS beam, two types of material failures may be initiated at these locations, i.e., tensile and shear failures. Among several failure criteria examined in the present work, i.e., the failure criteria defined by the maximum normal stress, maximum normal plastic strain, von-Mises equivalent stress, equivalent plastic strain, maximum shear stress, maximum plastic shear strain and the generalised plastic work density, only the last one appears to be suitable for predicting the initiation of a tensile type failure. Parametric verifications are conducted to ensure that the correct modeling for the material properties is used in the simulation.

Acknowledgements

The first author would like to acknowledge the financial support from the Impact Research Centre, The University of Liverpool. Other grants from the Christine King Memorial Trust, Henry Lester Trust, John Lennon Memorial Scholarship, the Great Britain–China Educational Trust and an ORS Award are also gratefully acknowledged.

References

ABAQUS, 1996. Theory and User's Manual/Standard, Version 5.5.

Alves, M., Jones, N., 1999a. Impact failure of beams using damage mechanics. Part I: analytical, Part II: application. Int. J. Impact Engng. (in press).

Alves, M., Jones, N., 1999b. Influence of hydrostatic stress on failure of axisymmetric notched specimens. J. Mech. Phys. Solids 47 (3), 643–667.

Bai, Y.L., Dodd, B., 1992. Adiabatic Shear Localization: Occurrence Theories and Application. Pergamon Press, London, UK.

Batra, R.C., Nechitailo, N.V., 1997. Analysis of failure modes in impulsively loaded pre-notched steel plates. Int. J. Plasticity 13, 291–308.

Batra, R.C., Gummalla, R.R., 2000. Effect of material and geometric parameters on deformations near the notch-tip of a dynamically loaded prenotched plate. Int. J. Fract. 101, 99–140.

Campbell, J.D., Ferguson, W.G., 1970. The temperature and strain rate dependence of the shear strength of mild steel. Phil. Mag. 21, 63–82.

Clift, S.E., Hartley, P., Sturgess, C.E.N., Rowe, G.W., 1987. Further studies on fracture initiation in plane-strain forging. In: Tooth, A.S., Spence, J. (Eds.), Applied Solid Mechanics-2. Elsevier, Amsterdam.

Clift, S.E., Hartley, P., Sturgess, C.E.N., Rowe, G.W., 1990. Fracture prediction in plastic deformation process. Int. J. Mech. Sci. 32, 1–17.

Cockcroft, M.G., Latham, D.J., 1968. Ductility and the workability of metals. J. Inst. Metals 96, 339.

Ferguson, W.G., Hauser, W.G., Dorn, J.E., 1967. Dislocation damping in zinc single crystals. Br. J. Appl. Phys. 18, 411–417.

Gillemot, L.F., 1976. Criterion of crack initiation and spreading. Engng. Fract. Mech. 8, 239–253.

Holmes, B.S., Kirkpatrick, S.W., Simons, J.W., Giovanola, J.H., Seaman, L., 1993. Modeling the process of failure in structures. In: Jones, N., Wierzbicki, T. (Eds.), Structural Crashworthiness and Failure. Elsevier Applied Science, London, pp. 55–93.

Johnson, G.R., Cook, W.H., 1983. A constitutive model and data for metals subjected to large strains, high strain rates and high temperatures. Proceedings of the 7th International Symposium on Ballistics. Am. Def. Prep. Org. (ADPA), The Hague, Netherlands, pp. 541–547.

Jones, N., 1989. Some comments on the modeling of material properties for dynamic structural plasticity. In: Harding, J. (Ed.), Mechanical Properties of Materials at High Rates of Strain. Institute of Physics Conference Series no. 102, pp. 435–445.

Jones, N., Shen, W.Q., 1993. Criteria for the inelastic rupture of ductile metal beams subjected to large dynamic loads. In: Jones, N., Wierzbicki, T. (Eds.), Structural Crashworthiness and Failure. Elsevier Applied Science, London, pp. 95–130.

Jones, N., 1997. Structural Impact, Paperback Edition. Cambridge University Press, Cambridge, UK.

Jouri, W.S., Jones, N., 1988. The impact behaviour of aluminium alloy and mild steel double-shear specimens. Int. J. Mech. Sci. 30, 153–172.

Kalthoff, J.F., 1990. Transition in the failure behaviour of dynamically shear loaded cracks. In: Chen, C.F. (Ed.), Proceedings of the 11th US National Conference of Applied Mechanics, Tucson, AZ, pp. 5247–5250.

Kalthoff, J.F., 2000. Modes of dynamic shear failure in solids, Int. J. Fract. 101, 1–31.

Kalthoff, J.F., Winkler, S., 1987. Failure mode transition at high rates of shear loading. In: Chiem, C.Y. et al. (Eds.), Proceedings of the International Conference on Impact Loading and Dynamic Behaviour of Materials. Bremen, Deutsche Gesellschaft fur Metallkunde, DGM, pp. 185–196.

Klepaczko, J.R., 1994a. Plastic shearing at high and very high strain rate. J. De Physique, Colloque C8, 35–40.

Klepaczko, J.R., 1994b. An experimental technique for shear testing at high and very high strain rates, the case of a mild steel. Int. J. Impact Engng. 15, 25–39.

Li, Q.M., 2001. Strain energy density failure criterion. Int. J. Solids Struct. 38, 6997–7013.

Li, Q.M., Jones, N., 1999. Shear and adiabatic shear failures in an impulsively loaded fully clamped beam. Int. J. Impact Engng. 22, 589–607.

Li, Q.M., Jones, N., 2000. On dimensionless numbers for dynamic plastic response of structural members. Arch. Appl. Mech. 70, 245–254.

Marchand, A., Duffy, J., 1988. An experimental study of the formation process of adiabatic shear bands in a structural steel. J. Mech. Phys. Solids 36, 251–283.

Meyers, M.A., 1994. Dynamic Behavior of Materials. John Wiley & Sons Inc, New York.

Ruiz, D., Harding, J., Ruiz, C., 1991. High-strain rate testing of materials—a fully validated test calibration by a hybrid numerical experimental technique. J. de Physique, III 1 (8), 465–470.

Rusinek, A., Klepaczko, J.R., 2001. Shear testing of a sheet steel at wide range of strain rates and a constitutive relation with strain-rate and temperature dependence of the flow stress. Int. J. Plasticity 17, 87–115.

Shen, W.Q., Jones, N., 1992. A failure criterion for beams under impulsive loading. Int. J. Impact Engng 12, 101–121, and 329.

Vinh, T., Khalil, T., 1984. Adiabatic and viscoplastic properties of some polymers at high strain and high strain rate. Institute of Physics Conference Series no. 70, pp. 39–46.

Woolman, J., Mottram, R.A., 1966. The Mechanical and Physical Properties of the British Standard En Steels, vol. 2. Pergamon Press, London.

Yu, J.L., Jones, N., 1997. Numerical simulation of impact loaded steel beams and the failure criteria. Int. J. Solids Struct. 34, 3977–4004.

Zbib, H.M., Jubran, T.S., 1992. Dynamic shear banding: a three-dimensional analysis. Int. J. Plasticity 8, 619–641.

Zhou, M.M., Rosakis, A.J., Ravichandran, G., 1996a. Dynamically propagating shear bands in impact-loaded pre-notched plates. I. Experimental investigations of temperature signatures and propagation speed. J. Mech. Phys. Solids 44, 981–1006.

Zhou, M., Ravichandran, G., Rosakis, A.J., 1996b. Dynamically propagating shear bands in impact-loaded prenotched plates. II. Numerical simulations. J. Mech. Phys. Solids 44, 1007–1032.